The Astrophysical Journal, 656:227–241, 2007 February 10

STRUCTURE GENERATION BY IRRADIATION: WHAT CAN GLIMPSE TEACH US ABOUT THE ISM STRUCTURE?

Fabian Heitsch,[1,2] Barbara A. Whitney,[3] Remy Indebetouw,[4] Marilyn R. Meade,[5] Brian L. Babler,[5] and Ed Churchwell[5]

Received 2006 July 10; accepted 2006 October 31

ABSTRACT

Diffuse emission in the mid-infrared shows a wealth of structure, which lends itself to high-resolution structure analysis of the interstellar gas. A large part of the emission comes from polycyclic aromatic hydrocarbons (PAHs), excited by nearby ultraviolet sources. Can the observed diffuse emission structure be interpreted as column density structure? We discuss this question with the help of a set of model molecular clouds bathed in the radiation field of a nearby O star. The correlation strength between column density and "observed" flux density strongly depends on the absolute volume density range in the region. Shadowing and irradiation effects may completely alter the appearance of an object. Irradiation introduces additional small-scale structure, and it can generate structures resembling shells around H II regions in objects that do not possess any shell-like structures whatsoever. Nevertheless, with some effort, structural information about the underlying interstellar medium can be retrieved. In the more diffuse regime [$n(\mathrm{H\ I}) \lesssim 100\ \mathrm{cm}^{-3}$], flux density maps may be used to trace the 3D density structure of the cloud via density gradients. Thus, while caution definitely is in order, mid-infrared surveys such as GLIMPSE will provide quantitative insight into the turbulent structure of the interstellar medium.

Subject headings: dust, extinction — infrared: ISM — ISM: structure — methods: numerical — radiative transfer — turbulence

1. THE PROBLEM

Diffuse emission in the infrared seems like a perfect laboratory in which to study the dynamics of the interstellar medium (ISM). Recent large-scale surveys by the *Spitzer Space Telescope*, specifically the GLIMPSE project (Benjamin et al. 2003), have provided us with unprecedented high-resolution data of the diffuse emission in the mid-infrared (MIR). At first glance the wealth of structure exhibited in the flux density maps seems a striking argument by itself for structure analysis.

However, the conspicuous structures themselves—namely, shells, bubbles, filaments, and dark clouds (see, e.g., Churchwell et al. 2004, 2006; F. Heitsch et al. 2007, in preparation; J. Jackson et al. 2007, in preparation; Mercer et al. 2006) raise the question of how much of the observed structure actually corresponds to physical structure. Flux density maps at any wavelength contain information about volume density, column density, and excitation, but it is possible to extract any of those quantities only under assumptions. For the structure analysis, we are ideally interested in volume density, which is accessible only indirectly, leaving us with column density as a second best at most. In fact, over a broad range of wavelengths, from ultraviolet to infrared, the opportunities seem to be rather rare in which we can interpret observed intensity maps of diffuse emission as information about the underlying column density structure. More often than not, the medium is optically thick for the emitted radiation or denser components of the ISM act as absorbers.

Optical depth effects become weaker with increasing wavelength, which is why the mid-IR ($\sim$5 μm) takes a somewhat special position (for a study of correlation between emission and column density in the far-IR, see, e.g., Bethell et al. 2004 and Schnee et al. 2006). At longer wavelengths from the far-IR through millimeter, current observatories have rather poor spatial resolution, precluding study of small-scale interstellar structure. With a dust/PAH extinction cross section of $C_{\mathrm{ext}} \approx 10^{-23}$ cm^2 per H atom (Li & Draine 2001a, 2001b; Draine 2003), the optical depth for MIR emission in molecular clouds should range below or around 1, which would encourage a direct interpretation of flux density as column density. For the near-infrared (NIR) this possibility has been discussed and supported by Padoan et al. (2006) to interpret so-called "cloudshine" observations by Foster & Goodman (2006), although in that case, the column densities would have to be substantially smaller than in the MIR.

Although applicable to a wider range of surveys, this paper focuses on the MIR diffuse emission as seen by the Infrared Array Camera (IRAC) on board the *Spitzer Space Telescope*. To a large extent, the emission in the [5.8] and [8.0] bands comes from PAHs (to a lesser extent they also contribute to the [3.6] band; Draine 2003), mostly excited in the environment of nearby UV sources.

Two (not unrelated) issues are raised in the MIR: (1) The medium is generally optically thick for the soft UV-radiation longward of 912 Å that excites the PAH emission. Thus, only the outer layers of any structures—unless really diffuse—are excited and thereby traced out in the MIR, giving the object a filamentary appearance. (2) Observationally, there seems to be a strong morphological bias to shells in the PAH emission. These could be dynamical shells (see Churchwell et al. 2006), e.g., wind-blown bubbles or H II regions. However, the destruction of PAHs around the UV source could also lead to a shell-like structure. Finally, these shells could be irradiation effects as noted under issue 1. And, of course, a combination of mechanisms is possible also. Moreover, the usual projection problem introduces a bias, so that observed structures can be interpreted as being two-dimensional (2D), when they could be very "three-dimensional" (3D): more diffuse material gets ionized or blown away first,

[1] Department of Astronomy, University of Michigan, Ann Arbor, MI; fheitsch@umich.edu.
[2] University Observatory Munich, Munich, Germany.
[3] Space Science Institute, Boulder, CO.
[4] Spitzer Fellow; Department of Astronomy, University of Virginia, Charlottesville, VA.
[5] Department of Astronomy, University of Wisconsin, Madison, WI.

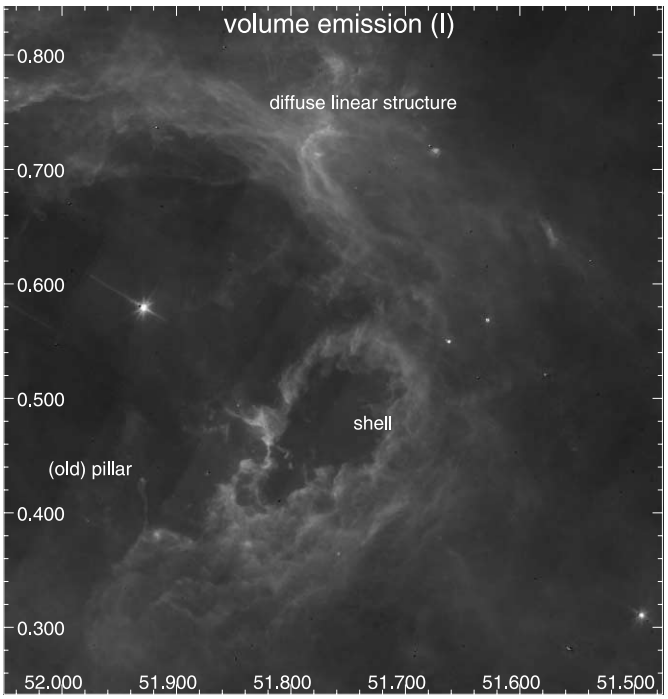

FIG. 1.—Residual image of diffuse emission at [8.0] μm, centered on $(l,\ b) = (51.8,\ +0.6)$.

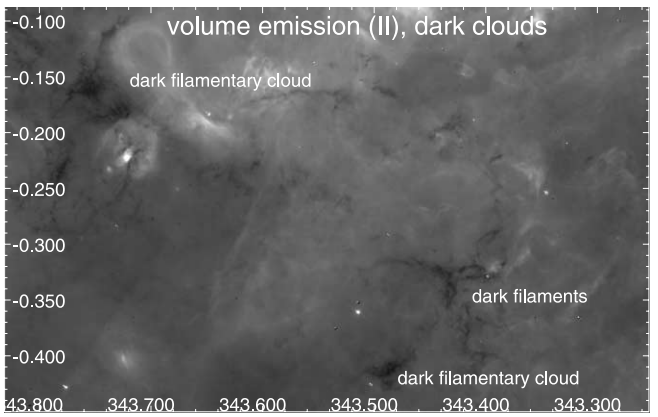

FIG. 2.—Residual image of diffuse emission at [8.0] μm, centered on $(l,\ b) = (343.5,\ -0.3)$.

leaving the ubiquitous elephant trunk remnant structures (for an impressive example of this problem, see the GLIMPSE study of RCW 49; Churchwell et al. 2004).

We investigate the appearance of a model molecular cloud in the radiation field of a nearby UV-source in order to quantify the correspondence of various measures and tracers between the original column density maps and the derived flux density maps. Rescaling the density range in the models allows us to mimic different physical environments, from diffuse clouds to dense molecular clouds and cores. The appearance of the original cloud can be completely altered by irradiation. Only for densities of up to $n(\mathrm{H\ I}) \approx 100\ \mathrm{cm}^{-3}$ can the flux density actually be interpreted as column density. Above that, MIR self-extinction and strong shadowing effects in the UV allow the maps to diverge. However, even for the highest density range [up to $n(\mathrm{H\ I}) = 10^5\ \mathrm{cm}^{-3}$], where the flux density maps bear no resemblance to the column density, the structural properties of the original column density distribution still can be retrieved from the flux density.

Our results demonstrate that the diffuse emission data as made available by GLIMPSE can serve as a powerful means to analyze the (dynamical) structure of the ISM in selected regions. This study aims at pointing out possible pitfalls and at giving a rule-of-thumb estimate of where flux density structure could be trusted to represent column density. In the next section (§ 2) we give some observational motivation in the form of diffuse emission maps from the GLIMPSE data. We are deferring the full structure analysis of the GLIMPSE data to a future paper. The models and the details of the radiative transfer treatment are described in § 3. The results (§ 4) are summarized in § 5.

2. OBSERVATIONAL MOTIVATION

The following maps are extracted from images of the GLIMPSE project. The data were processed through the GLIMPSE pipeline reduction system (Benjamin et al. 2003; Whitney et al. 2004). Point sources were extracted from each frame using a modified version of DAOPHOT (Stetson 1987). Subtracting the point sources leads to residual images, which then were mosaicked. Only sources fit well by a stellar point-spread function (PSF) were extracted. Thus, saturated and near-saturated stars remain in the images. In addition, there are some artifacts resulting from point-source subtractions due to the undersampling of the stellar PSF at IRAC wavelengths. Figures 1–5 show [8.0] residual mosaic images displayed in Galactic coordinates. We split the maps into three categories: volume illumination (§ 2.1), absorption and shadowing (§ 2.2), and high-density environments (§ 2.3).

2.1. *Volume Illumination: Optically Thin in the UV*

Figures 1 and 2 show two examples of "volume-filling" diffuse emission, i.e., the optical-depth effect described in § 1 does not seem to be the dominant structure generation mechanism. Rather, it seems, the diffuse emission traces the volume density. While Figure 1 shows a clear shell-like structure, Figure 2 exhibits dark filaments, probably extinction in the MIR against a bright diffuse background. The apparent volume illumination could either stem from material that is optically thin for the exciting UV provided by a nearby star or by the interstellar radiation field (Fig. 2), or arise in an environment that—although at higher densities—contains several UV-sources, so that we still see large parts of the volume in PAH emission (Fig. 1).

2.2. *Dark Clouds: Absorption and Shadowing*

Figures 3 and 4 give two examples of structures that are typical of the GLIMPSE data: the combination of bright and dark features in one and the same object.

In Figure 3, the (Galactic) north side of the filament is seen in emission, while the south side shows dark structures. Figure 4 displays a structure composed of bright vertical filaments, which may be an example of volume illumination (see previous section), possibly the remainder of a larger shell, while the object in question is located at smaller longitudes l than the filament, at $(l,\ b) = (309.04,\ -0.42)$: the left side is emitting, while the right side is seen as dark structure. In contrast, the top of the same figure shows a "pure" dark cloud, without any irradiation features. The reader will find more examples in the other frames. This raises the question of whether we are seeing two physically distinct classes of objects here, or whether the "bright-dark" clouds are just an illuminated version of the classic dark clouds. The bright-dark clouds can often be associated with irradiating sources (see F. Heitsch et al. 2007, in preparation), so that we identify the two morphological classes as one and the same type of object, namely, dark clouds.

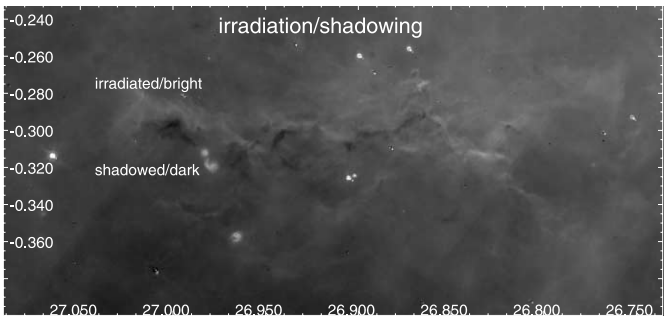

FIG. 3.—Residual image of diffuse emission at [8.0] μm, centered on $(l,\ b) = (26.9,\ -0.3)$. Dark absorption regions are predominantly located on the southern side of the filament.

The combination of dark and bright clouds is also observed optically (e.g., in the Ophiuchus cluster), with filamentary dark clouds streaming off a bright region.

2.3. *High-Density Environments*

The region around $(l,\ b) = (30.7,\ 0.0)$ (Fig. 5) shows one of the many bubbles in the GLIMPSE data (Churchwell et al. 2006). Bright dust/PAH emission and dark clouds form an intricately structured network. The northern part of the bubble exhibits several shell-like structures, whose brightness tapers off to the diffuse background more or less immediately. The region is compact and contains a lot of dark extinction regions in the bright emission regions, indicating that this is a high-density environment. Note, however, that darker regions in emission could also just mean that the PAHs have been destroyed around the UV source. Volume illumination seems to play less of a role here; instead, the rim effects mentioned in the introduction seem to have come into full play.

3. IRRADIATION OF A MODEL CLOUD

3.1. *The Simulations*

We used two model series: series A is meant to resemble star formation regions in the Galactic disk. It is derived from cloud dispersal models in a turbulent flow (Heitsch et al. 2006) and corresponds to a box length of 44 pc, a background density of 0.5 cm^{-3}, and a cloud density of 150 cm^{-3}. Model A is in approximate pressure equilibrium, with a temperature of 9500 K in the ambient medium. The model is not self-gravitating.

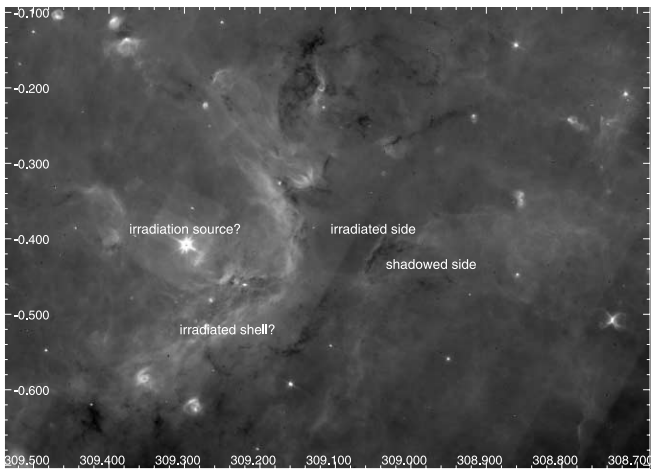

FIG. 4.—Residual image of diffuse emission at [8.0] μm, centered on $(l,\ b) = (309.1,\ -0.4)$. At $(l,\ b) = (309.00,\ -0.42)$, there is a bright-dark cloud. A pure dark cloud can be found at the top of the frame.

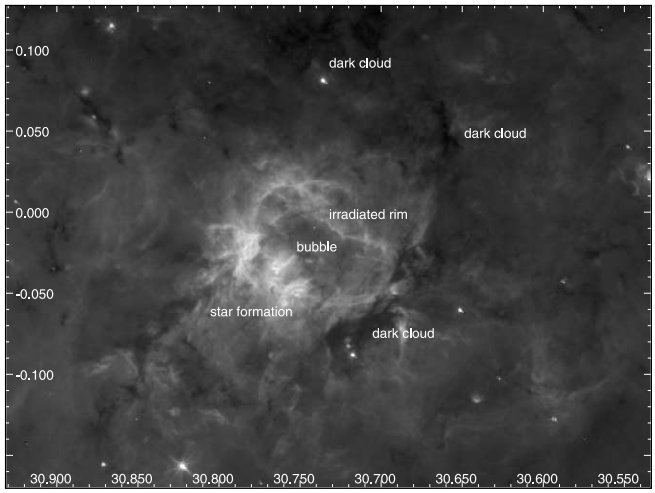

FIG. 5.—Diffuse emission at [8.0] μm, centered on $(l,\ b) = (30.7,\ -0.0)$. The UV sources (sites of star formation) in the southern part of the structure irradiate the surrounding remains of the molecular gas (possibly the parent molecular cloud).

Series B stems from self-gravitating MHD-turbulence models in a periodic box (Heitsch et al. 2001a, 2001b). It is intended to be typical for conditions within a molecular cloud, with a box size of $\approx$3 pc and a mean density of 1000 cm^{-3}, an (isothermal) temperature of 10 K, and a turbulent rms velocity of 1 km s^{-1}. As we see below, self-gravitation has already lead to core formation.

Both model series A and B have a resolution of 256^3 grid cells. The density contrast can be adapted to test irradiation effects in various environments.

3.2. *UV Source and Ray Tracing*

The UV-source is assumed to be a O5 V star that can be placed anywhere in the simulation domain. Note that we are just investigating the radiation paths of the stellar UV photons. The models do not account for ionization or stellar winds and thus cannot provide us with estimates how they would affect the emission structure. We further assume that only UV photons with $\lambda > 912$ Å are available for PAH excitation, and that photons with shorter wavelength have already been absorbed within the H II region around the star. We follow the photons on rays through the simulation domain. The discretization in longitude and latitude follows the HealPix prescription (Górski et al. 2005) in order to guarantee equal areas for each ray. Rays are traced within a tree-structure such that optical depths are known locally at each node of the tree. The number of rays is determined by the number of cells on a sphere with radius r (in grid cells) as $N_{\rm ray} = 4\pi r^2$. Thus, each cell on a given sphere gets at least one ray. Densities are interpolated trilinearly on the Cartesian grid.

For each location (r, θ, ϕ), the energy loss is determined by

$$dL = L(r) - L(r + dr) = \frac{4^{-l}}{12} L_0 \left(e^{-\tau(r)} - e^{-\tau(r+dr)}\right), \quad (1)$$

with the central (stellar) luminosity L_0 and the local optical depth (measured from the UV source)

$$\tau(r) = \int_0^r n(\mathrm{H\ I}) C_{\rm abs}\, dr, \quad (2)$$

where n(H I) is the atomic hydrogen particle density, and $C_{abs} = 1.0 \times 10^{-23}$ cm^2 is the PAH absorption cross section per H atom. The factor $4^{-l}/12$ accounts for the ray splitting: The base level consists of 12 rays, each of which spawns 4 children at the next refinement level l. The radial step size is dr, thus the volume at each location is known, and dL can be multiplied by the corresponding volume expression, resulting in the actual UV-energy loss. We integrated over the whole UV-spectrum of the incident radiation field between 912 and 3000 Å (see, e.g., Li & Draine 2001b; Fig. 1) with the constant absorption cross section C_{abs} given above. Furthermore, we assume that all UV-energy absorbed by the PAHs is converted into PAH emission, which we distribute according to the PAH-spectrum by Draine (2003) also consistent with Draine & Li (2006). As shown by Li & Draine (2001b) the spectrum is independent of the radiation field over a large range in intensity. The emitted spectrum, sampled at 30 wavelengths, is convolved with the IRAC response function (Reach et al. 2006) for band 4 at [8.0] μm, which contains the bulk of the PAH emission (Draine 2003). The resulting "gray" emission is integrated along the line of sight (i.e., along a chosen grid axis) following the equation of radiative transfer, including emission and extinction, with an extinction cross section $C_{ext} = 1.2 \times 10^{-21}$ cm^2 per H atom.

We keep the dust/PAH ratio fixed. Therefore, we do not consider the destruction of PAHs close to the central source, i.e., PAHs are to be found everywhere in the simulation domain. Although this is a somewhat artificial scenario, it allows us to isolate structure generation purely caused by the underlying gas density distribution, not by PAH abundances (see § 4.1 and Figs. 8 and 9).

The chosen absorption and extinction cross sections C_{abs} (0.2 μm) and C_{ext}(8 μm) are a factor of ≈1.5 smaller than the values given by Li & Draine (2001a, 2001b) and Draine (2003) (see also Draine & Li 2006). They give values of $C_{abs} \approx 1.5 \times 10^{-21}$ cm^2 and $C_{ext} \approx 1.4 \times 10^{-23}$ cm^2. The slightly smaller cross sections can be accommodated by rescaling the density. Note, however, that in both cases the cross sections for UV and MIR differ by a factor of 100. Thus, material which is optically thick at UV can be optically thin at the reemitted MIR. In fact, it is to a large extent this difference that leads to the wealth of structure in the observed MIR diffuse emission. Because of the large opacity difference, we do not expect the approximation of constant cross sections over the wavelength bands considered to affect our results.

4. RESULTS

The irradiation effects will alter the appearance of the cloud, depending on gas density and geometry (§ 4.1). The (point) source needs to be subtracted (§ 4.2) to permit a meaningful analysis of the spatial structure (§ 4.3) and to facilitate a test of the traditional structure analysis tools, namely power spectra (§ 4.3.1) and structure functions (§ 4.3.2). The overall correlation between column density and flux density deteriorates with increasing volume density (§ 4.4). Under certain conditions, the flux density maps can even be used to trace the 3D structure of the cloud (§ 4.5).

4.1. *Morphologies*

We begin by discussing the morphology of the irradiated objects depending on the source's position and the density contrast. The appearance of the irradiated cloud depends strongly on the absolute gas density and on the location of the source.

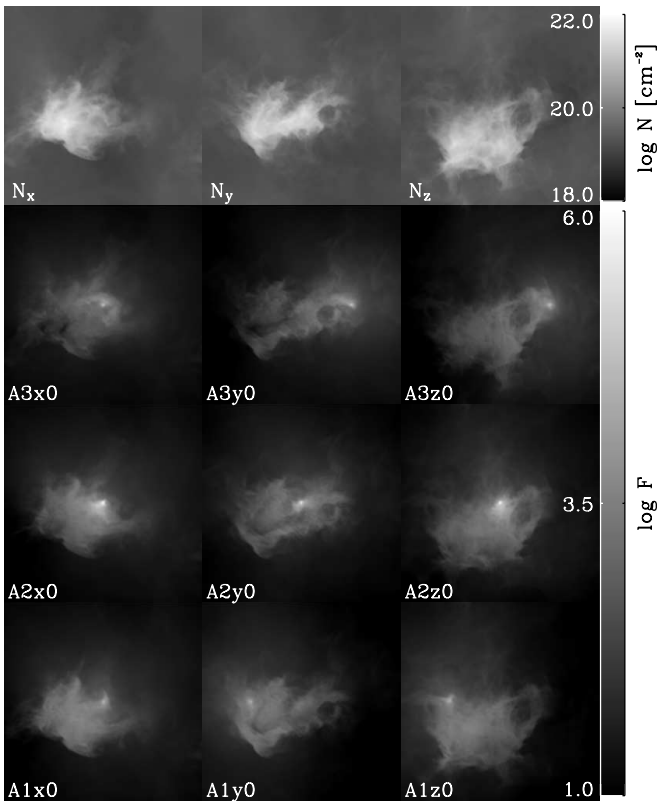

FIG. 6.—Irradiated cloud (model A??0) seen along the three coordinate axes x, y, and z. The top row gives the column density in units of square centimeters. The star is shifted through the volume along the x-axis (see text). The flux units are arbitrary. The density contrast is 1. Shown are maps corresponding to the IRAC band 4. The key to the label names is as follows: First digit: model series (here: A). Second digit: stellar position in units of $L/4$ along the x-axis: A value of 1 stands for the star being located between observer and cloud (*bottom left*), 2 for at the box center, and 3 for the star behind the cloud, as seen along the x-axis. Third digit: coordinate axis parallel to line of sight. Fourth digit: logarithm of density contrast. The actual gas density ranges from 1 to 10^2 cm^{-3}.

4.1.1. *Irradiated Cloud*

Figures 6–9 give a first impression of the appearance of an irradiated cloud. The top row of each figure shows the column density along each of the three Cartesian axes. Each column stands for one of the Cartesian axes along which the pictures have been taken. The first digit of the labels in the panels gives the model series name (A or B). The second digit stands for the position of the star along the x-axis in units of $L/4$, where $L = 44$ pc is the box length. A value of 1 in the first column of images means that $\frac{1}{4}$ of the box length is between the observer and the star, e.g., panel A1x0 represents a situation where the source is located between observer and most of the cloud, and thus the cloud "face" in the plane of sky as seen by the observer is irradiated. Thus, in the left column, the star is moved along the line of sight, and in the center and right columns, it is moved from left to right. The cloud itself is contained in approximately the central half of the box. The third digit (x, y, z) gives the Cartesian coordinate axis along which the model has been projected. The last digit denotes the logarithm of the density contrast enhancement above the contrast already existing in the simulation, i.e., a value of 2 denotes a density contrast enhancement of 10^2. Thus, columns are a sequence in position, rows are a sequence in line-of-sight orientation, and each of the four Figures 6–9 contains frames of a fixed density contrast. The densities range between 1 cm^{-3} at the edge of the box (in the "intercloud medium") and 10^2 cm^{-3}

TABLE 1
Model Names

Digit			
First (1)	Second (2)	Third (3)	Fourth (4)
Series: (A, B)	Position: 1 = near 2 = center 3 = far	Projection axis: *x*, *y*, *z*	Density contrast: log ($\Delta n/\Delta n_0$)

Notes.—Col. (1): Model series A corresponds to an isolated cloud; model series B stands for a periodic box of driven, self-gravitating MHD turbulence. Col. (2) Position of illuminating source within box, along the *x*-axis. Col. (3) Projection axis for flux density maps derived from 3D models. Col. (4) Enhancement of density contrast over model-intrinsic value.

within the cloud for a contrast enhancement of 1, and between 1 and 10^3 cm^{-3} for a contrast enhancement of 3. Question marks in the model names act as group specifications, e.g., "A??0" refers to all panels in Figure 6, whereas "A?x0" refers to the panels at varying star position, projected along the *x*-axis (i.e., Fig. 6, *left*). The model names are summarized in Table 1.

For a density contrast of 1 (Fig. 6), the cloud's column density structure is well traced by the PAH emission. The object is still optically thin enough for the UV photons to excite its whole volume. Panel A3x0 and the row A?y0 show slight self-extinction of the PAH emission (slightly darkened regions within the cloud). The model sequence A??0 could be compared to Figures 1 and 2.

The extinction structures get more pronounced at the next higher density contrast of 10 or a density range $1 < n(\mathrm{H\ I}) < 10^3$ cm^{-3} (Fig. 7). Panels A??1 tell us more about these regions:

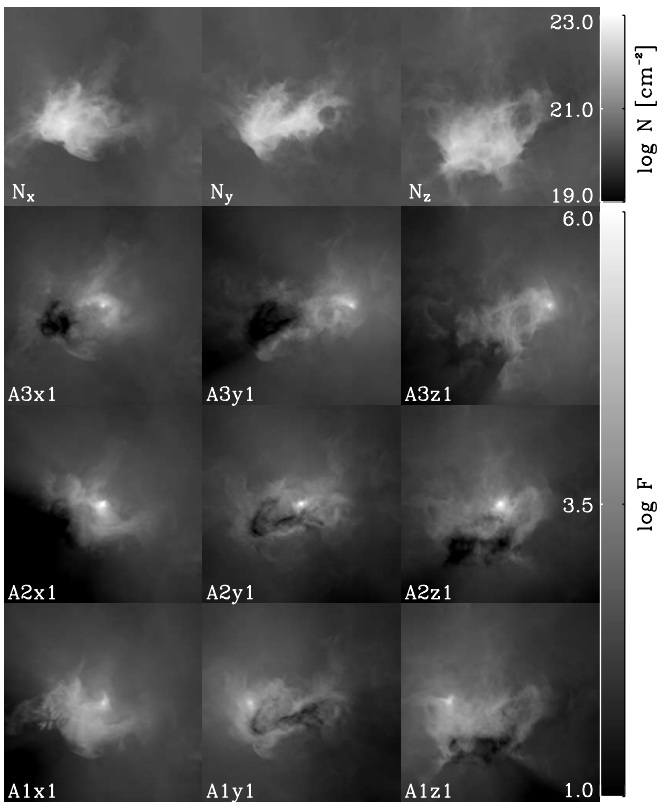

Fig. 7.—Same as Fig. 6, but for model A??1, and with a density contrast of 10 and actual gas density ranging from 1 to 10^3 cm^{-3}.

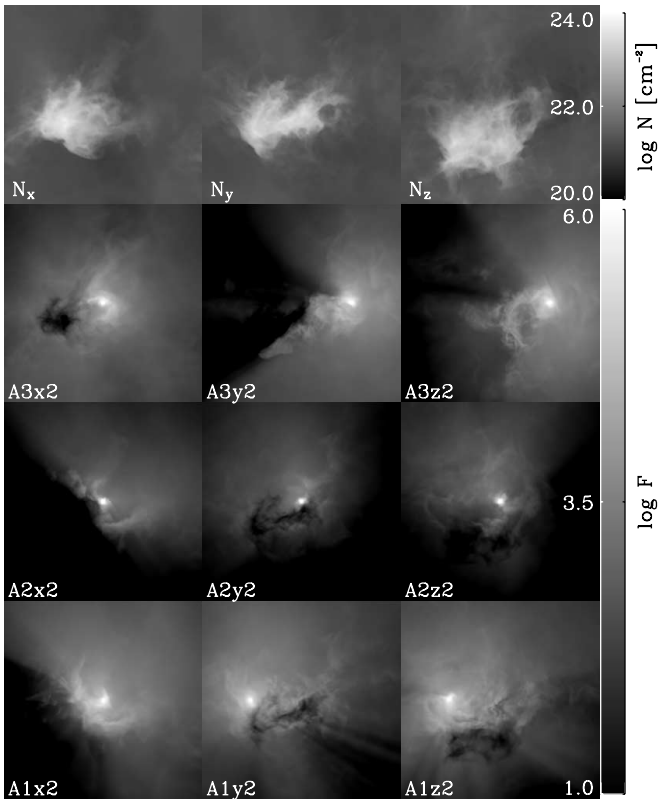

Fig. 8.—Same as Fig. 6, but for model A??2, and with a density contrast of 100 and actual gas density ranging from 1 to 10^4 cm^{-3}.

The dark structures are a combination of UV absorption *and* MIR extinction. Since the star is moving away from the observer from panel A1x1 to panel A3x1, the dark fuzzy region in A3x1 must be located between the star and the observer. If it were solely due to UV-absorption, it should show up as a "bright" (light gray) region in the PAH emission. The fact that it is dark in the PAH emission maps thus shows that it is not only a UV shadowing effect, but that it is also dense enough to extinct the background MIR radiation. A similar effect can be seen in panel A3z1, at the lower left of the cloud. The region is UV-shadowed by the bulk of the cloud, however, in contrast to A3x1, the optical depth in the MIR is smaller, so that while the background MIR is extincted, its brightness is close to the background brightness. As one can see in the corresponding column density map above A3z1, the region is still within the cloud, i.e., there remains gas available for extinction of the MIR. A wisp of denser gas in front of the shadowed region is irradiated by the source, showing up in lighter gray. The effect of the background intensity will be discussed for the model series B.

Increasing the density contrast further to 100, corresponding to a density range of $1 < n(\mathrm{H\ I}) < 10^4$ cm^{-3} (Fig. 8, *panels A??2*) leads to stronger absorption, and in some cases to complete shadowing. Simultaneously, the diffuse gas—still mostly optically thin for the UV photons—gets brighter. Overall, the maps seem to be more "structured" than their lower density counterparts, which is partly an effect of the combination of emission and extinction, and partly because at higher densities, smaller changes in density are traced out.

That shadowing effects play a large role can be seen in Figures 7 and 8 (models A??1 and A??2). Moreover, the spatial structure of the cloud continues from the emission regions to the extinction regions (panel A1z2), an effect often seen in the diffuse emission maps (see the examples in § 2.2 as well as F. Heitsch et al. 2007, in preparation).

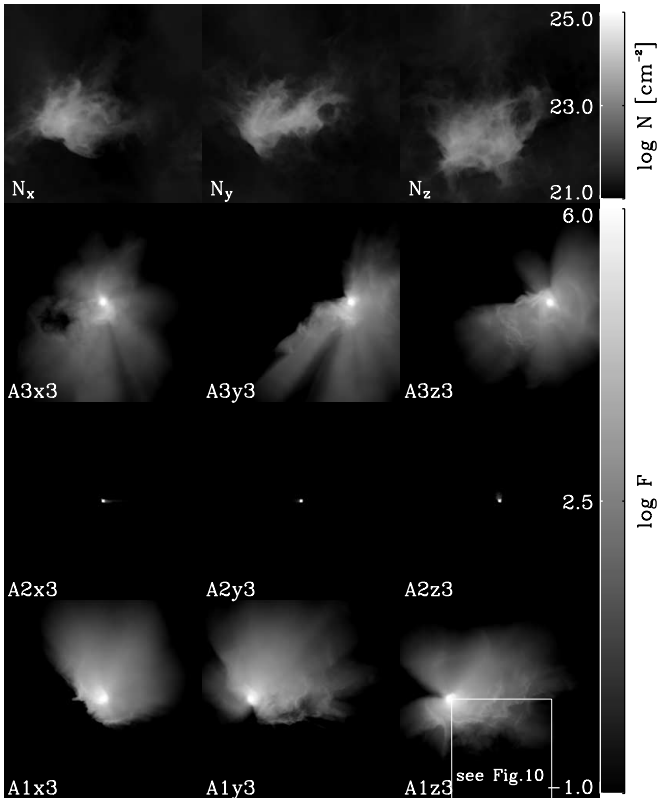

FIG. 9.—Same as Fig. 6, but for model A??3, and with a density contrast of 1000 and actual gas density ranging from 1 to 10^5 cm^{-3}. The box in panel A1z3 denotes the region studied in Fig. 10.

Figure 9, panels A??3 stands for the extreme case: It corresponds to a molecular cloud with densities ranging up to 10^5 cm^{-3}. Except for the close vicinity around the star, the object stays dark: all the UV is absorbed directly (see row A2[x, y, z]3). In panel A3?3, we actually catch a glimpse of the far side of the cloud: the irradiating source is on the far side of the cloud, and while the cloud is optically thick to the exciting UV, it is still (marginally) optically thin for the PAH emission. The "dark fuzzy" region discussed in A3x1 is still visible and has acquired a "halo" of excited PAHs.

The irradiation by the central star introduces shell-like patterns in an object that does not have any shell structure whatsoever (see column density panels at top of Figure 9): Especially, panel A1z3 gives the impression of a star sitting in a 3D shell, of which only the lower right part is visible. In other words, it is relatively simple to confuse such structures with the signposts of interaction between a star and its surrounding medium (although – obviously – it does not rule out such an interaction). This situation reminds one of the irradiated shell-like structure at (l, b) = (309.15, −0.45) in Figure 4, labeled "irradiated shell?"

Figure 10 presents a closer look at a subregion of panel A1z3—marked by the box in panel A1z3 of Figure 9–in order to learn more about the mechanisms that lead to the shell-like structures in the flux density maps. The two center panels show the column density and the flux density, where the central source is now located in the upper left corner of the frames. The shell-like structures appearing in Figure 9 are indicated by dashed lines in the flux density panel of Figure 10. The top and bottom panels show column and flux density profiles for two rays indicated on the gray-scale maps. Vertical lines denote local maxima in the flux density, marked as well on the gray-scale maps by short vertical lines. Generally, we would expect emission peaks at locations where the radial volume density gradient is positive, and its

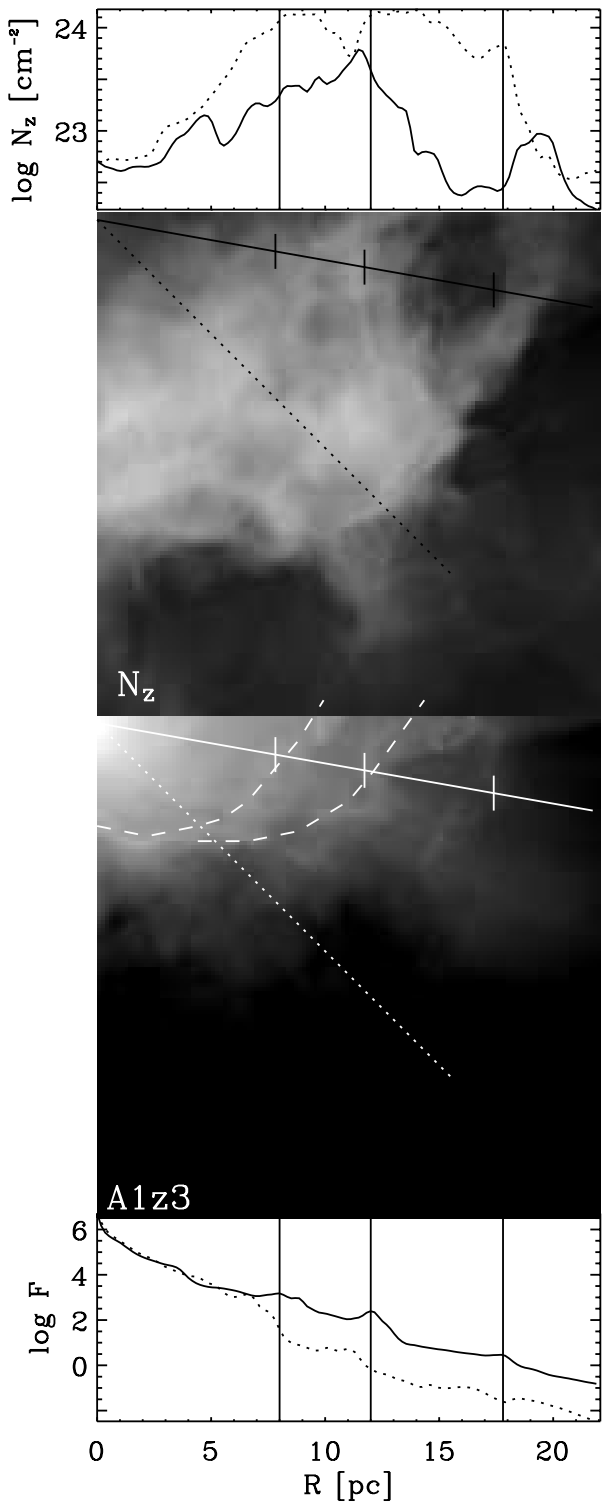

FIG. 10.—Model A1z3 in a zoomed-in view (see box markings in Fig. 9). The central source is now located in the top left corner. Overplotted are two rays through the column density and flux density map respectively, whose profiles are shown in the top and bottom panel. Vertical lines denote points of local maxima in the flux density along the ray. In order to help identification in the maps, these points are marked with small vertical lines on the ray. Not all flux density maxima have corresponding column density maxima. The two more prominent shell-like structures visible in panel A1z3 of Fig. 9 are indicated by dashed lines in the flux density map.

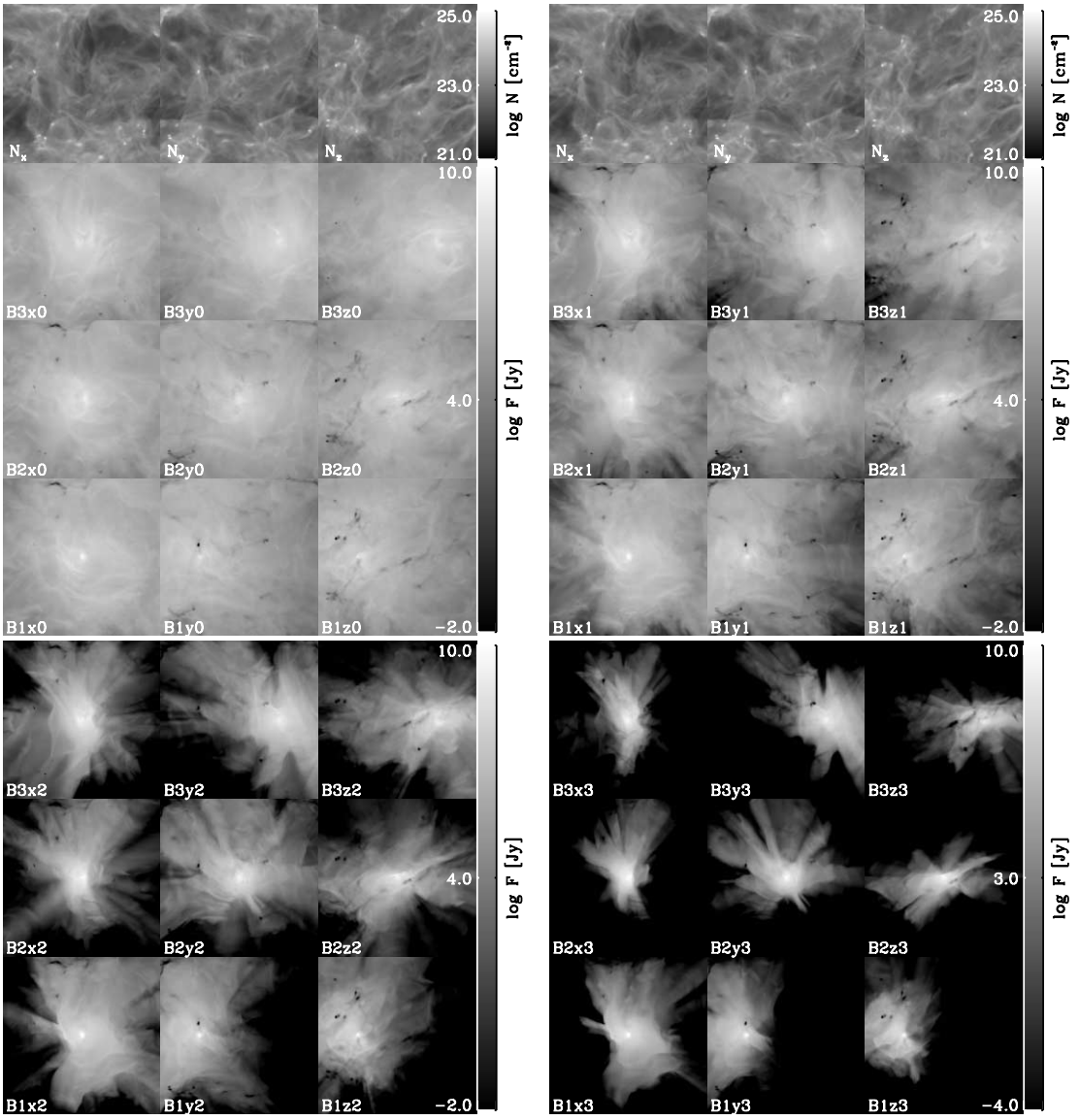

FIG. 11.—Same as Fig. 6, but for model B, and with density contrasts of 1, 3, 10, and 30.

curvature negative. However, of the three locations, one does not follow this expectation: we observe an emission peak for a negative *column* density gradient. Since enhanced emission can only occur at positive radial density gradients, this might seem surprising, but it only tells us that the flux density maps in fact trace out the 3D structure of the cloud: while the overall column density drops with increasing distance from the source, a local density enhancement (most likely in the foreground because otherwise it would be masked) leads to the peak in the flux density. Thus, the shell-like structure observed here has nothing to do with a physical shell, but is a result of a lucky combination of smaller density enhancements predominantly located in the foreground. Observationally, such objects could be distinguished from physical shells by comparing them at other wavelengths, e.g., in the dust continuum at 24 μm. We have to mention a caveat here, though. Our models do not account for PAH destruction in the vicinity of the star. This would introduce a further bias toward shell-like structures, independent of any dynamical effects such as stellar winds or H II regions.

While the overall resemblance between observed flux density maps and the modeled ones (e.g., A??2) is suggestive, there is nevertheless one striking difference: The modeled maps exhibit dark radial streaks caused by the total absorption of UV and thus the lack of PAH emission along those rays. Such structures are generally not observed, for the following reasons: (1) In the observed maps, the lines of sight through the Galaxy are substantially longer than in the model cubes, and thus diffuse material in the foreground and/or background will lead to a much higher uniform flux, which easily would cover any faint low-brightness structures. (2) The restriction to one source and neglecting the interstellar radiation field introduces a directional bias in our models which then leads to the shadows seen in the models. Only if the absorbing material is located directly between the observer and the source are shadowing effects likely to be observed in a typical location of the Galactic ISM, namely, as dark clouds.

Clearly, the overall correspondence between column density maps and the PAH emission maps deteriorates for increasing densities.

4.1.2. *Embedded Star*

Figure 11 is a variation on the previous theme, namely flux density maps of a self-gravitating turbulent medium, irradiated

by a star. As before, a sequence in increasing density contrast is shown. One difference between model A and B is obvious: Model B does not exhibit a well-defined irradiated cloud structure (or at least the rims of that). One could see model B as a "close-up" of model A, taken of a small region around the star inside the cloud of model A. In model B, the UV-radiation is mainly stopped by the numerous filaments arising from shock compressions. In addition to those filamentary structures, the emission has a "foglike" appearance: in contrast to model A, the density within the cloud is already high enough to absorb sufficient UV to trace even low-density regions, and the scales of the frame are smaller by a factor of nearly 15, so that we are seeing the close environment around the O star. The small black objects visible at the higher density contrasts are self-gravitating cores that have already collapsed. While it is possible to identify irradiated filaments with structure in the column density map (*top*), the overall agreement between flux density and column density (even for the lowest contrasts) is rather poor. The densities range between 10 and $10^4 \mathrm{cm}^{-3}$ in the original density distribution (density contrast enhancement of 0, model B??0). An enhancement of 1 then corresponds to a maximum density of 3×10^4 cm^{-3}, 2 to 10^5 cm^{-3}, and finally 3 to $3 \times 10^5 \mathrm{cm}^{-3}$.

The bottom row of Figure 11 would correspond to an embedded UV source in a high-density environment. The closest observational correspondence is shown in Figure 5. In both cases, the dense gas leads to dark regions (in the models) or clouds (in the observations). However, already the differing shapes tell us that the dark regions arise for different reasons: the observed dark regions stem from back-illumination by the diffuse 8 μm emission along the whole line of sight, while the dark raylike regions in model B are a result of the complete UV-absorption of the single source available in the model.

Model sequence B does not seem representative of observed diffuse MIR emission. The column density maps prominently exhibit filamentary structure over the whole domain. These filaments are shock fronts caused by the supersonic turbulence in the box. However, they are not reproduced in the flux density map. Obviously, because of their highly transient nature, the filaments contain only little mass, so that they do not represent a major obstacle to the star's UV-radiation. Stars form in these models predominantly in the (abundant) intersections of filaments. The high shock compression leads to a close to instantaneous destabilization and fragmentation of these intersections, resulting in the formation of collapsed cores after less than one dynamical time in the simulations (see, e.g., Klessen et al. 2000; Heitsch et al. 2001a). In other words, cores form too soon in these simulations for the filaments to gather sufficient mass to be seen in MIR diffuse emission.

4.2. *Intensity Distributions*

Before we can quantitatively analyze the intensity distributions (this section) and the spatial structure (§ 4.3), we need to "remove" the central source, which would otherwise dominate the analysis. To that purpose, we average the intensities azimuthally, centered on the flux density peak, and subtract the resulting profile from the frame. An alternative approach would be to just cut off the peak of the intensity corresponding to the central source. However, this leaves the imprint of the R^{-2} dilution of the radiation field, which is a direct effect of the central source and would confuse the structure analysis. The subtraction of the R^{-2} profile could be seen as a modified photometry algorithm for point sources irradiating a surrounding, optically thin diffuse medium.

The residual frame (Fig. 12) still shows artifacts due to the central source, but the cloud structure is more pronounced than in the "directly observed" maps. Comparing the residual maps

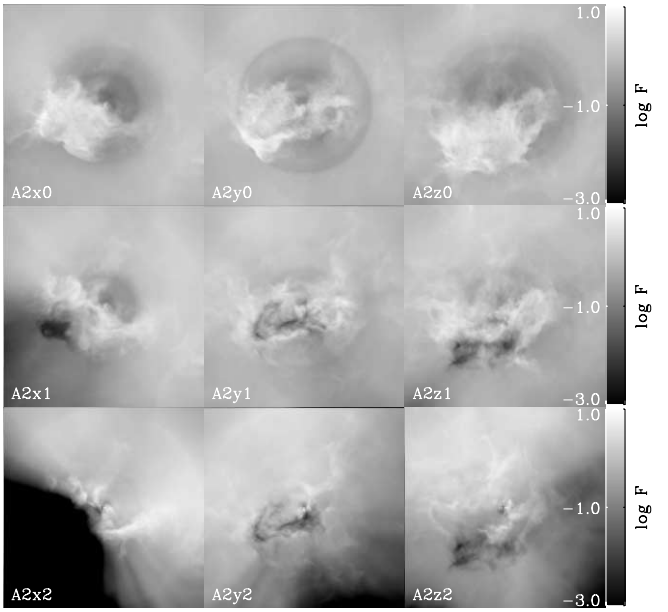

FIG. 12.—Residual flux density maps for the three lower density contrasts of model A. Artifacts unfortunately are unavoidable.

to the column density maps (Figs. 6–9, *top row*) demonstrates that the *irradiation*—besides introducing additional structure via absorption (dark regions)—*generates more small-scale structure than observable in the column density map*. This is mostly an optical depth effect in the sense that already small increases in the optical depth (shocks, filaments, and smooth gradients in the density) leads to additional absorption which then will be traced out by the reemitted MIR. This effect gets amplified if the "obstacle" uses up all the remaining UV photons in that ray, i.e., if the optical depth changes from $\tau < 1$ to $\tau \gg 1$ within that structure. The result is a bright region facing the central source and a dark, shadowed region facing away from the source.

Subtracting the central source in model B (Fig. 13) is not as prone to produce artifacts in the residual flux density maps because the model is pretty much isotropic by construction. In contrast, since the cloud center of model A does not coincide with the UV source, artifacts are unavoidable, which are easily recognized as darker circular regions.

4.3. *Spatial Structure*

In the previous section we saw that a "byeye" comparison of the column density maps and the flux density maps reveals additional structure in the flux density. The next two sections discuss under which conditions and how strongly the irradiation affects structure measures. We test the reliability of two traditional structure analysis tools, namely, power spectra (§ 4.3.1) and structure functions (§ 4.3.2). Since the flux density maps at higher densities are dominated by global irradiation effects, power spectra are a less suitable tool for structure analysis than structure functions, where masking is possible. The latter can only be trusted if applied to small enough regions not to be influenced by global irradiation effects.

4.3.1. *Power Spectra*

Power spectra offer a convenient method to study the structure of complete (i.e., unmasked) data. The power spectrum of a flux density map F is defined as

$$P(k) \equiv \hat{F}(k)\hat{F}(k)^* = \hat{\mathrm{AC}}(k), \tag{3}$$

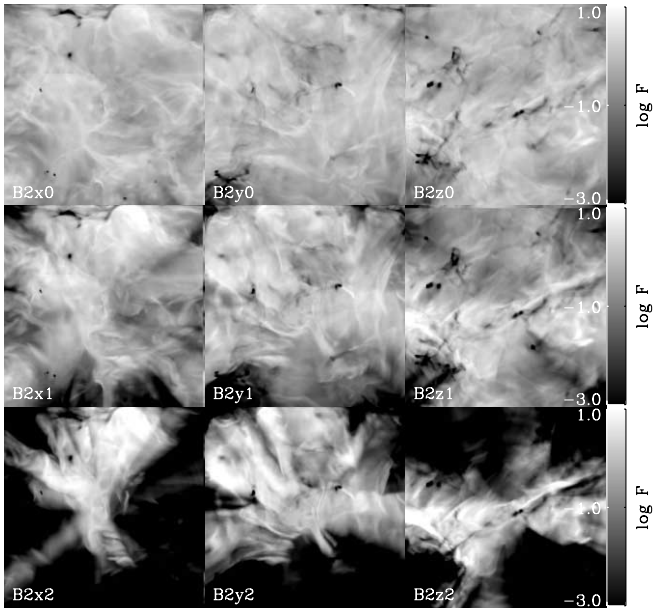

FIG. 13.—Residual flux density maps for the three lower density contrasts of model B. Since the model tends to be more isotropic by construction, artifacts of the subtraction carry less weight.

where $\hat{F}(k) = \int e^{ikx} F(x)\,dx$ is the Fourier transform of F with complex conjugate $\hat{F}(k)^*$, and $\hat{\mathrm{AC}}(k)$ is the Fourier transform of the autocorrelation function

$$\mathrm{AC}(l) \equiv \langle F(x)F(x+l)\rangle_x. \tag{4}$$

How reliable is the structure information extracted from diffuse emission? Figure 14 gives an impression for our irradiated cloud (model A). The top panel shows the power spectrum for the original column density map, without any source or irradiation. The three lower panels in turn give the spectra of the irradiated cloud including the source (*solid lines at top of panels*), and the spectra of the residual flux density, i.e., with the central source subtracted as described in § 4.2. Obviously, the maps including the source are completely useless for structure analysis: the source dominates the whole spectrum. The slope ranges around -0.2 (not shown in the plot). A completely different picture is revealed when analyzing the residual maps: The resulting slopes approach the values of the column density maps. *The slightly flatter slopes indicate that irradiation introduces additional small-scale structure.* The artifacts introduced by the subtraction of the central source in model A2?0 are mirrored in the slight hump of the corresponding spectrum around $\log k \approx 0.9$. Note that the power-law exponents refer to power spectra, i.e., a Kolmogorov law would be represented by $-10/3$.

To conclude for model sequence A, the power spectra reproduce the original scale distribution within the errors, which however are substantial, due to the circular averaging.

The situation changes drastically for model series B (Fig. 15), because the high-density cores lead to a strong power increase at small scales (basically, they act as noise) in the column density spectrum, which is why this spectrum is much flatter than expected for a turbulent power spectrum (see also Heitsch et al. 2001a for a discussion of this effect). Note that the column densities in the cores range approximately 2 orders of magnitude above the mean column density (Fig. 11). Since only a tiny fraction of a dense core can emit in the MIR, these objects generally

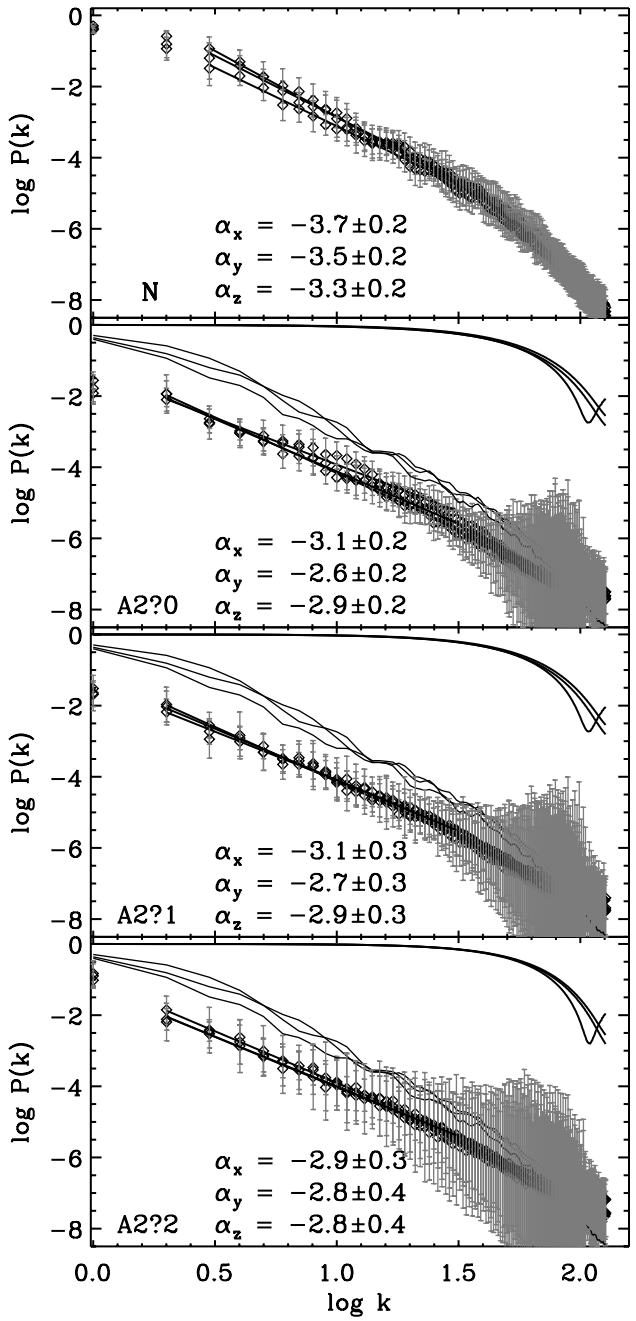

FIG. 14.—Power spectra of column density (*top*) and flux density (*remaining panels*) for models A2?0 through A2?2. All spectra are normalized to the mean. Symbols with error bars stand for measured spectra of the column density (*top*) and for the residual maps (*bottom three panels*), while the thick solid lines around $\log P(k) = 0$ in the bottom three panels correspond to the spectra of the maps including the central source. The three thin solid lines stand for the power spectrum of the column density shown in the top panel. The fitted power-law exponents $\alpha_{x,y,z}$ are given in the panels, where the indices denote the direction of the line of sight (e.g., α_x belongs to A?x2). The error bars denote the logarithmic error on the mean, while the errors in α contain the fit error as well as the error on the mean.

do not show up in the emission maps, and then only in extinction. Again, the central source dominates the "uncleaned" spectrum. Thus, since the high-density cores do not contribute strongly in the flux density map but give a strong signal in the column density map, the MIR maps of model B are preferable for structure analysis if one aims at excluding strong point-source signals.

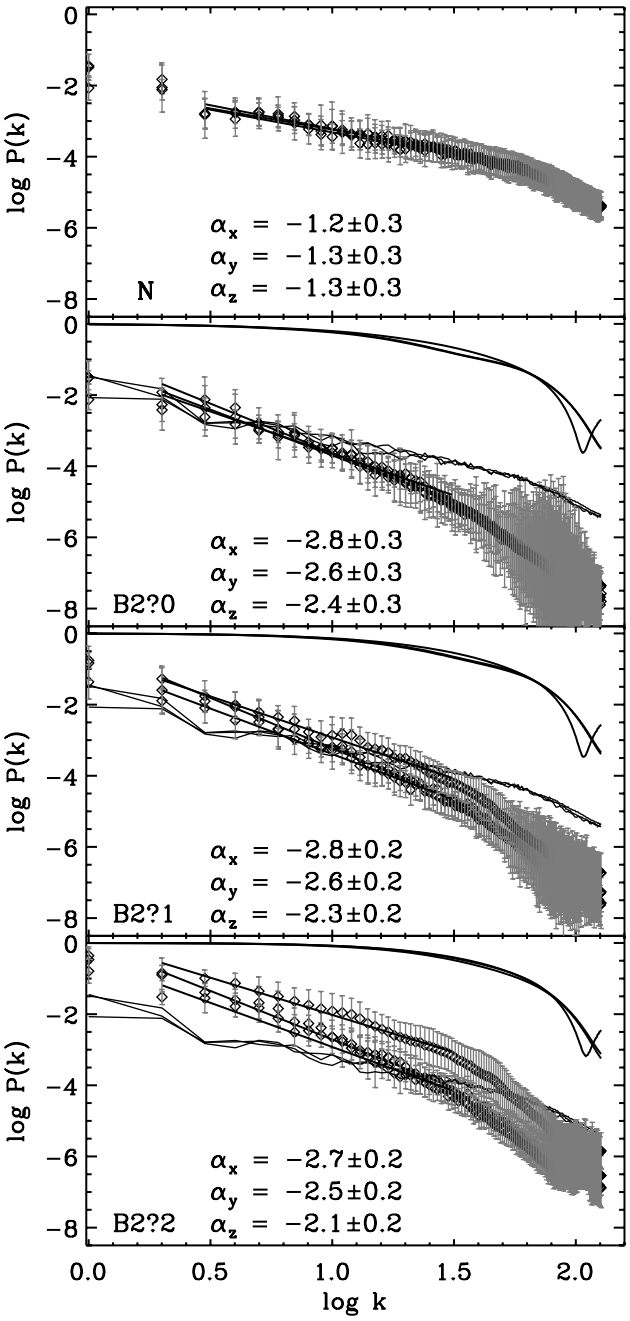

FIG. 15.—Same as Fig. 14, but for models B2?0 through B2?2.

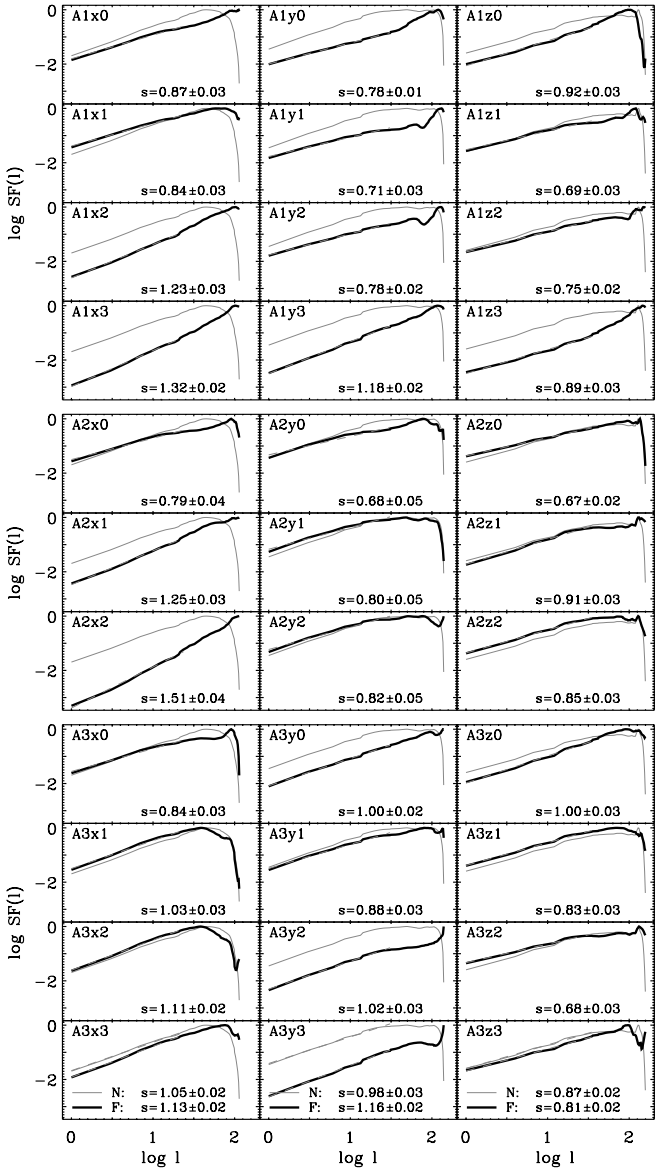

FIG. 16.—Structure functions of column density $N > 10^{22}$ cm^{-2} (*thin lines*) and residual flux density maps (*thick lines*) for the three Cartesian directions. The four top rows belong to models A1??, with the source being offset to smaller *x*. The three center rows refer to model A2??, with the source dead center, and A3?? is represented by the four bottom rows, where the source is offset to larger *x*. Thick lines denote the structure function of the residual flux density map, and thin lines stand for the structure function of the original column density maps. Since model A2?3 would not be very revealing (see Fig. 9), we dropped it. See Table 1 for definition of model names.

4.3.2. *Structure Functions*

Structure functions are a more appropriate tool for analyzing the spatial distribution of an incomplete data set, since masking introduces artificial signals in the power spectra. Only pixels with a measurable signal would contribute to structure functions of observational data. However, due to the irradiation and absorption effects the flux density map generally will not cover the whole cloud, as demonstrated in § 4.1. Thus, in order to compare the column density and flux density maps, we selected the former for column densities $N > 10^{22}$ cm^{-2}, which traces out the bulk of the cloud. Applying the resulting mask to the flux density maps and determining the (second order) structure functions

$$\mathrm{SF}(l) = \langle |F(x) - F(x+l)|^2 \rangle_x \qquad (5)$$

with lag l and spatial coordinate x, results in Figure 16. The structure function SF is related to the autocorrelation (eq. [4]) and the power spectrum (eq. [3]) via

$$\mathrm{SF}(l) = \langle F(x)^2 \rangle_x - 2\mathrm{AC}(l). \qquad (6)$$

The four top rows belong to model A1??, with the source being offset to smaller *x*. The three center rows refer to model A2??, with the source dead center, and A3?? is represented by the four bottom rows, where the source is offset to larger *x*, so that A3x? refers to a configuration in which the cloud is located between observer and source. Each panel shows the structure function of the original column density at $N > 10^{22}$ (*thin line*).

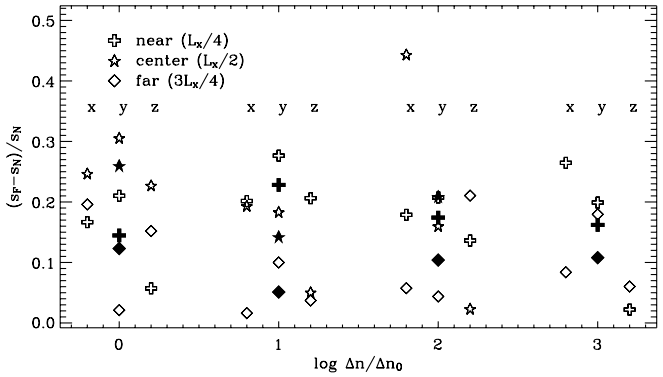

FIG. 17.—Normalized difference between logarithmic slope of structure functions (eq. [7]) for column density (s_N) and flux density (s_F), against the density contrast. For reasons of clarity, the three coordinate directions are plotted in open symbols centered around their respective density contrast, i.e., A?x1 can be found left of $\Delta n/\Delta n_0 = 1$, A?y1 at 1, and A?z1 right of 1. Filled symbols denote the mean over the axis directions x, y, and z. Symbol types refer to the position of the source as indicated in the top left. "Near" means "near end of the box," i.e., closest to the observer, while "far" means that (most of) the cloud is located between the observer and the irradiation source. See Table 1 for definition of model names.

The structure function for the corresponding flux density is plotted in thick line style. The numbers s in each panel refer to the logarithmic slope of the structure function,

$$\log \mathrm{SF}(l) \propto l^s, \tag{7}$$

taken over the first decade in l. Although a column density threshold of $N > 10^{22}$ leads to most of the high-density gas in one contiguous object, there are a few isolated cloud fragments. Since these cloud fragments are separated from the main body of the cloud, they tend to have the largest lags with respect to the main body, however, it turns out that their column densities are close to the mean column density within the main body, so that the structure functions show a drop at large lags. Since Figure 16 is somewhat messy to interpret, Figure 17 summarizes the degree to which the original column density structure information is retrieved from the flux-density maps, quantified by the difference between the logarithmic slopes of the structure functions for column density s_N and for flux density s_F, normalized by s_N.

Just looking at the filled symbols (averages over the three coordinate directions) one might get the impression that *larger* density contrasts lead to more accurately retrieved slopes. This is somewhat surprising. However, the scatter between the three coordinate directions is substantial and suggests to take a closer look at Figures 6–9 again.

As shown in § 4.5, the lowest density contrast allows a "volume rendering" of the cloud: the medium is optically thin enough so that the exciting UV can light up the whole cloud, nearly acting as a uniform background field. If the source is within the cloud, though, it tends to overrepresent the volume directly around it. Thus, the best fit is given by A3y0, where the source is located seemingly at the tip of a filament, farthest away from the bulk of the cloud. The effect of overemphasizing close-by structures can be well observed even in A3y0: above the source, a filament is traced out that does not show up clearly in the column density map. Comparing this to A3x0, we see that it suffers from "neighborhood illumination" by the source: internal structure of the cloud thus is just smeared out: the flux-density slope is flatter than the column density slope (Fig. 16). A3z0 fares slightly better, although here the source overemphasizes the ringlike structure close by, leading to a steeper slope. The center-position maps (A2?0) all suffer from the source being located inside the cloud, while models A1?0, where the source (seen along the x-axis) is located in the front, again tell a mixed story. For A1z0, the source is located at the upper left end of the cloud, in a fairly diffuse environment and sufficiently far away from the bulk of the cloud in order not to affect the structure function (*third cross symbol for* $\log \Delta n/\Delta n_0 = 0$ in Fig. 17). For A1x0 and A1y0, the source is already too embedded.

Moving on to the next density contrast, $\log \Delta n/\Delta n_0 = 1$, again A3y1 shows the lowest deviation; however, because of the shadowing effects in the cloud's left ("eastern") part, the deviation is larger than for A3y0. That A3x1 provides better fits than A2x1 and A1x1 is understandable again because of shadowing, although it is not directly clear why the match should be better than that for A3x0. Checking the corresponding panels A3x0 and A3x1 in Figure 16 gives the answer: on the small scales, the structure functions agree, while on large scales they differ. The better matches for A1z1 and A2z1 (compared to A3z1) might be a consequence of the shadowed regions, which still show substructure: *this substructure would enter the structure function on the small scales and provide the same information as structure in emission.* Thus—granted that we chose a small enough field for analysis—to some extent structure in absorption and emission can be used simultaneously for analysis.

At density contrasts $\log \Delta n/\Delta n_0 = 2$ and 3, matching between the overall shapes of structure functions for column and flux density deteriorates on the large scales (Fig. 16), as one would expect by looking at Figures 8 and 9. However, there is still enough signal from irradiating small density variations for the structure functions to match on the small scales. Again, given that we take a small enough region, the structure function can be reproduced.

Another limitation on the size of the region is given by the available dynamic range in the observed flux density maps. In the diffuse emission, it often turns out that the dynamic range is spanning one, at most two, decades, which limits the spatial scales available for analysis.

To summarize, structure functions seem to be a much more viable tool to investigate localized diffuse emission than power spectra. Despite the fact that the irradiation sometimes modifies the underlying density information beyond the point of recognizability, the resulting structure functions still retrieve the salient scale information—given that the field investigated is small enough. Because of the global irradiation effects, there is only little hope to retrieve the large-scale information accurately. The most promising way would be to identify small, "uncontaminated" regions and reconstruct the structure information from those.

The deviations (Fig. 17) are within the errors on the mean of the structure function (see the analysis of power spectra). Again these stem from the circular averaging. The large deviations in fact point to a major problem when applying two-point correlators to data exhibiting anisotropic structures. For example, filaments will lead to different structure information along and perpendicular to their long axis, in turn leading to a mixing of the spectral information when averaging the directions. Since the observed structure in the interstellar medium seems to be anisotropic to a large extent, the application of unmodified two-point correlators might raise questions. We will discuss this problem and possible remedies in a future paper.

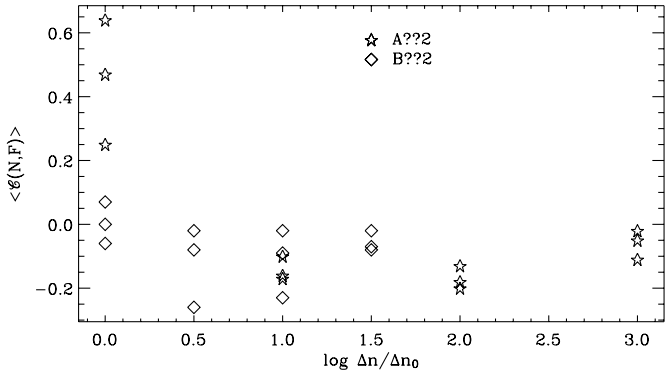

FIG. 18.—Correlation coefficient (eq. [8]) for model series A and B. For larger density contrasts, the maps are uncorrelated. Negative values denote anticorrelation; positive values denote correlation.

4.4. *Correlation Measures*

How reliably are structures in column density reproduced in the flux density maps? The correlation coefficient

$$\langle \mathcal{C}(N,\ F)\rangle \equiv \frac{\sum (N_{ij}-\langle N\rangle)(F_{ij}-\langle F\rangle)}{\sqrt{\sum (N_{ij}-\langle N\rangle)^2}\sqrt{\sum (F_{ij}-\langle F\rangle)^2}} \tag{8}$$

serves as a first crude estimator for the similarity of column density maps N_{ij} and flux density maps F_{ij}. The means over the map are denoted by $\langle N\rangle$ and $\langle F\rangle$, respectively. For all density contrasts larger than 1, N and F are basically uncorrelated (Fig. 18).

The correlation coefficient provides an overall estimate for how "similar" the maps are. Unfortunately, equation (8) is only of limited use for a point-to-point similarity measure. Although one could plot a map of the summands, the normalization is unclear. One possible similarity measure is given by

$$\mathcal{C}(N,\ F) \equiv \frac{N-\langle N\rangle}{\langle N\rangle}\frac{F-\langle F\rangle}{\langle F\rangle}. \tag{9}$$

At locations in which both maps show either strong or weak signals, $\mathcal{C} > 0$, while positions with anticorrelated signals will exhibit $\mathcal{C} < 0$.

Figure 19 shows $\mathcal{C}(N,\ F)$ for model A. It can be directly compared to Figures 6–8 and 12 For the lower density contrasts, the column density map correlates well with the emission (*light gray to white shades*), while for higher density contrasts, the absorption regions lead to a strong anticorrelation. The overall positive correlation deteriorates for larger density contrasts.

4.5. *PAH-Emission as Edge Sensor*

If the UV from the central source excites PAH emission in the rims of the surrounding molecular cloud, the emitted flux density could be used as an edge sensor or gradient indicator. To test this, for each position in the simulation domain and the column density map we calculate the 3D radial density gradients

$$\partial_R \rho(R_{i,j,k},\ \theta_{i,j,k},\ \phi_{i,j,k}) \equiv \left(\frac{\hat{\rho}-\rho}{\Delta R}\right)_{i,j,k}, \tag{10}$$

and the 2D column density gradients, respectively,

$$\partial_r N(r_{i,j},\ \phi_{i,j}) \equiv \left(\frac{\hat{N}-N}{\Delta r}\right)_{i,j}. \tag{11}$$

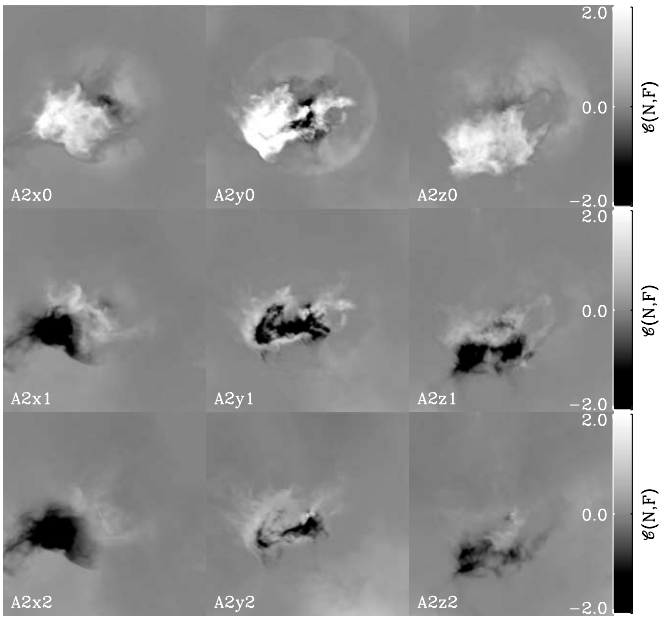

FIG. 19.—Correlation maps (eq. [9]) for model series A. Negative values (*black*) denote anticorrelation, while positive correlation is indicated by positive values (*white*). Anticorrelated regions generally mean high column density and strong absorption.

The hatted quantities are linear interpolations of the (column) density at the positions

$$\hat{\rho} \equiv \rho(X_i + \Delta R \sin\theta\cos\phi,\ Y_i + \Delta R \sin\theta \sin\phi,\ Z_i + \Delta R\cos\theta); \tag{12}$$

$$\hat{N} \equiv N(x_i + \Delta r\cos\phi,\ y_i + \Delta r \sin\phi), \tag{13}$$

with $R \equiv (X^2+Y^2+Z^2)^{1/2}$ and $r \equiv (x^2+y^2)^{1/2}$. The radial increments ΔR and Δr measure one grid cell, and θ as well as ϕ in equations (12) and (13) refer to the coordinates $(i,\ j,\ k)$, $(i,\ j)$, respectively. The gradients are computed with respect to the central source ($R = 0$ and $r = 0$ at position of source) and selected for positive values (Figs. 20, 21). Positive gradients $\partial_R \rho > 0$ indicate locations of enhanced UV-absorption and thus enhanced PAH-emission, while $\partial_r N$ would denote the same if the physical cloud structure were truly 2D. We compute $\partial_R \rho$ and $\partial_r N$ for each cell in the simulation domain and column density map respectively, i.e., A slight subtlety enters regarding the 3D case: We still need to project the gradients on a plane. In order to keep the 3D information at least partially, we color-coded the distance along the line of sight, where blue colors denote short distances (toward the observer) and red colors denote long distances (at the far end of the volume). The intensity gives the strength of the gradient. The distance information is weighted with the gradient strength, i.e., two gradients of same strength located at one quarter and at three quarters of the box length will show up in purple.

We focus on Figure 20 (models A2?1 and A2?2) first. The top row shows the original column density, followed by the 2D gradient $\partial_r N$ and the projected 3D gradient $\partial_R \rho$. The two bottom rows give the flux density maps for models A2?1 and A2?2, i.e., for increasing density contrast. The color scale is a measure of the location of the gradient, with blue closest to the observer, and red at the far end of the box. Clearly, the gradients making

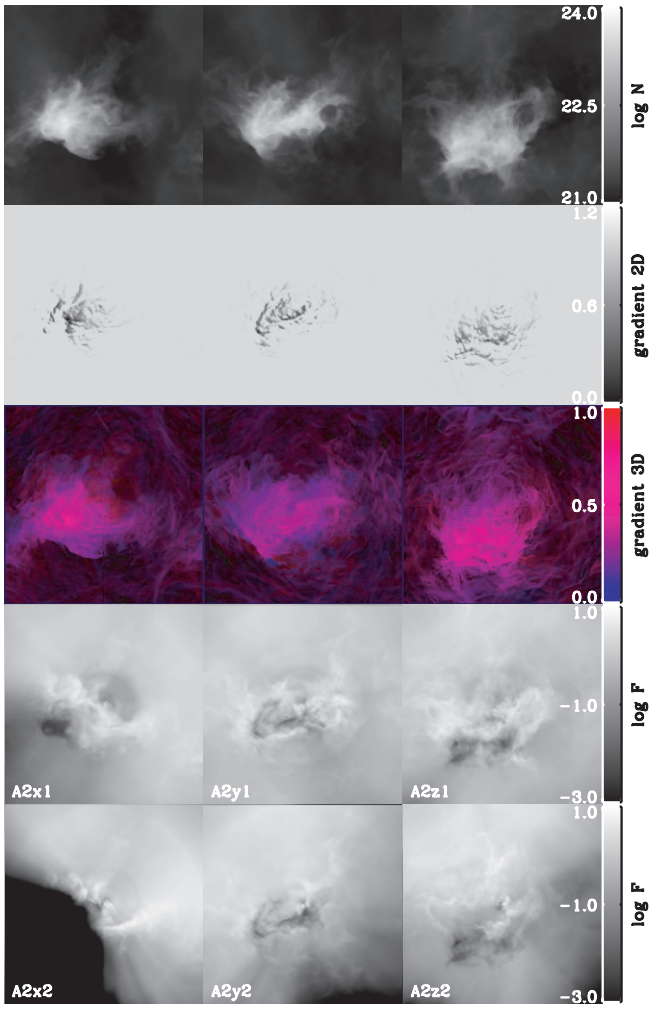

FIG. 20.—Gradient maps (see text) for model A, source centered (A2??). Column density (*top row*) and flux density (*two bottom rows*) are shown for comparison. The color bar for the 3D gradient gives the distance along the line of sight in box units, with 0.0 (*blue*) closest to the observer, and 1 (*red*) located at the far end of the box.

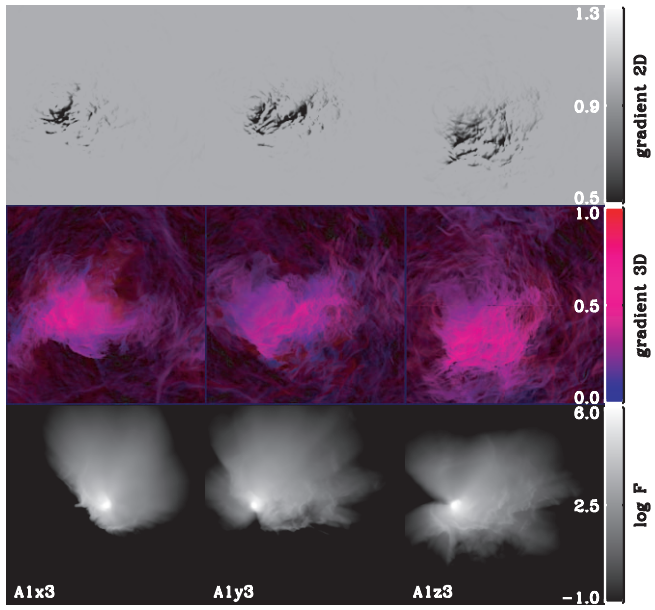

FIG. 21.—Gradient maps (see text) for model A, source at position 1 (A1??).

up the map come from all possible locations along the line of sight. Taking A2y1, the L-shaped structure visible in extinction in the flux-density maps is traced out by a hazy bluish gradient indicator: The corresponding density jump is close to the observer, which makes sense, since dense material between the source and the observer leads to the extinction. Farther to the right of the L-shape, the gradient map of A2y? shows a red (albeit dark) region: weak gradients at the far side of the source. Correspondingly, we see a bright irradiated region in the flux density map of A2y1: the (far away) structures are irradiated by the central source. This is not seen anymore in A2y2: the density has increased and leads to extinction of the far-away emission. Similarly, the dark region to the lower left of the center in A2x1 corresponds to gradients close to the observer. In this case however, there is no clear blue signal in the 3D gradient map, which indicates that the dark region is caused by a combination of UV shadowing and MIR extinction of diffuse background. Moving northward of that direction, the source of emission is receding from the observer: again, this information is lost at higher density contrast (A2x2), and thus the cloud structure is only incompletely "sampled." Interestingly, for A2z2, the situation is nearly converse: the dark gradient-regions link up with strong emission signals (to upper left of the center), while the extincted regions to the south are farther away from the observer. Thus, those dark regions might again be caused by a combination of missing irradiation and extinction of diffuse background. The "handle" to the right is located at the far side of the central source.

Compared with this richness of structure, the 2D gradients come as sort of a big disappointment: they resemble the cloud structure only in the widest sense. Beginning with A2y1 again, the L-shape is recovered, but this is already all we can see. For A2z?, the handle to the right of the central source is showing up slightly in $\partial_r N$. However, moving to the larger density contrast (A2?2), the situation changes slightly: the flux density maps look more "rim"-like, more easily identified with the 2D gradient map. Carrying this idea to the extreme, Figure 21 shows the gradient maps and flux densities for A1?3 (as Fig. 9 shows, model A2?3 would be not exactly informative in this context). The 3D gradients now are hardly reproduced (with the noticeable exception of the Southern absorption rim in A1x3). The 2D gradients however tend to trace now the absorption rims (see, e.g., A1y3 and A1z3). *Thus, for lower density contrasts, or a more diffuse environment, the emission structures are intrinsically 3D, while for higher density regions, they tend to get more and more 2D* (*although 3D effects are still not to be neglected*).

5. SUMMARY

The abundance of structure in MIR diffuse emission as observed in, e.g., the GLIMPSE data seems to offer a perfect laboratory to study the dynamics of the dense ISM. However, a large part of the observed structure could be irradiation effects due to PAH emission. PAHs are excited by UV photons from nearby stellar sources or the interstellar radiation field, and reemit in the MIR. Because the respective cross sections differ by a factor of approximately 100, material, which is optically thick in the UV, can still be optically thin in the (emitted) MIR. Thus, PAH emission is often seen in filamentary structures, probably the "rims" of denser clouds. These irradiation effects might spoil the opportunity to study the ISM gas structure, since this requires interpretation of the observed flux density in terms of volume or column density. Motivated by a few examples taken from GLIMPSE, we identified possible limitations of this interpretation. We quantified the reliability of flux-density maps of

diffuse emission in the MIR to reproduce the underlying (column) density information. We used two model sets, one corresponding to a (more or less) isolated "molecular" cloud, and the other imitating a region deep inside a molecular cloud, both irradiated by an O5 star. PAHs absorb the UV and reemit the energy in the MIR, which then is integrated along the line of sight, including MIR extinction. In the following, we will summarize how reliable flux density maps reproduce column density in our models, and how this affects the structure analysis, with possible applications to MIR observations.

5.1. *Morphology: Column Density and Flux Density*

If the medium is optically thin for the irradiating UV, then the MIR emission maps could be used for a high-resolution study of the column density structure of the medium. Padoan et al. (2006) supported this possibility for the NIR, based on the observations of "cloudshine" by Foster & Goodman (2006). Since they were interested in the appearance of the diffuse emission, they used an isotropic radiation field mimicking a UV background, in contrast to our models that employ a point source for irradiating the surrounding medium. Considering the abundance of UV sources and the presence of a diffuse UV background, we are thus taking a "worst-case" approach. For higher density environments such as molecular cloud in the vicinity of strong UV sources, interpreting MIR emission as column density requires considerable caution: The transition from $\tau < 1$ to $\tau > 1$ can lead to strong signals in the MIR flux density, but not necessarily paired with a corresponding signal in the column density: At large τ, the maps bear no resemblance to the column density (Figs. 6–9 and 11). In the extreme case PAH emission is only excited at the rims of clouds (e.g., Churchwell et al. 2006), causing the impression of a highly filigree structure in the gas: irradiation introduces more small-scale structure than observable in the underlying column density maps. As soon as shadowing is obvious, the structure seen in emission will generally not represent column density. The shadows (especially radial dark streaks) are not seen in observed data, indicating that observed clouds are generally not illuminated by just a single source. Some of the observed shell-like structures could be just irradiation effects, and by themselves indicate that shadowing (or "rimming") has set in (Figs. 5, 7, and 10). Since our models do not include PAH destruction around the star, we expect them to exhibit fewer shell-like structures than observed. PAH cavities would lead to "shells" even if the cavities were not associated with, e.g., wind-blown bubbles.

5.2. *Structural Properties*

Power spectra are only partially useful for an analysis of diffuse emission structure. Their well-known main drawback is that they tend to confuse the information about extent of a region and the separation of regions. Furthermore, masking is always an issue in power spectra, since it tends to introduce a signal by itself. Power spectra containing the central source are completely dominated by that (Fig. 14), while spectra of residual maps are slightly flatter than the underlying column density distribution. This could be a projection effect and/or the result of additional small-scale structure traced out by irradiation. The spectral slope is pretty much insensitive to the density contrast within the error bars, which are significant. For collapsed regions (Fig. 15), the column density spectrum flattens considerably because of the strong point source contribution. Compared to that, the flux density spectra steepen because the point sources are not fully irradiated and thus do not show up (except in extinction).

Structure functions seem to be a more viable tool to investigate localized diffuse emission. Despite the fact that the irradiation may modify the underlying density information beyond the point of recognizability, the resulting structure functions still retrieve the salient scale information—given that the field investigated is small enough not to be contaminated by global irradiation effects. There is little hope to retrieve the *large-scale* information accurately by applying a global structure measure such as power spectra. Structure in extinction can be used as a continuation of structure seen in emission, although this raises the issue of an appropriate choice of background for the extincted region (Figs. 3 and 7). The deviations (Fig. 17) are within the errors on the mean of the structure function.

Since the overall structure in the ISM tends to be anisotropic, applying two-point correlators seems at least questionable. Averaging in k- or l-space leads to substantial errors on the mean, which themselves indicate that the underlying structure is anisotropic to a large extent.

The application of these results to actual observational data (GLIMPSE) and the discussion of anisotropy we defer to a future paper.

5.3. *Flux Density as Gradient Indicator*

Since the conversion of UV to MIR will occur predominantly at regions of large positive radial density gradients (as long as there are UV photons left), the flux density maps might offer the opportunity to gather information about the (3D) density structure of the cloud. To test this, we compared the radial volume and column density gradients to the flux density maps. For lower density contrasts, the flux density maps tend to trace out the 3D structure of the cloud, and in fact they can be used as 3D gradient indicators. For higher density contrasts, they revert to an indicator of the column density gradients: the structures seemingly become 2D. Thus, more diffuse regions appear "more 3D," while higher density environments tend to be 2D.

5.4. *Limitations*

Beside the irradiation effects discussed here, there are other limitations to an interpretation of flux density maps as column density.

1. If the volume density is low enough that the exciting UV can irradiate the whole cloud, one might question how long the line-of-sight actually is, and whether angular effects leading to scale-mixing in a structure analysis would play a role. Thus, structure analysis of the diffuse MIR emission is best done at larger Galactic longitudes, where the lines of sight through the Galactic disk are limited, and where there might be a chance to determine the distance of the studied structure (e.g., via H II regions).
2. On the other hand, the volume density might be large so that the irradiating UV will be absorbed more or less directly "at the rim" (if such a thing exists) of the cloud. Then, depending on the geometry of observer, irradiated medium and irradiation source, the observer might see predominantly one-dimensional or 2D structures, implying projection effects in the spectral information.
3. The scenario studied here represents the "worst case" since we consider irradiation by one single point source. This is highly unrealistic, considering the interstellar radiation field and multiple UV sources, but it leads to a strong spherical bias in the PAH-emission. The fact that we see the "shadowing" rays is one indicator of this problem: If there were additional sources outside the cloud, these shadows would vanish, and geometry effects in the irradiation might play less of a role. Thus, while the single-source geometry is a limitation of the models

presented here, it may well work in our favor when analyzing observed maps.

5.5. *Conclusions*

Depending on the diagnostics, MIR flux density maps of diffuse emission from PAHs excited by a nearby UV source can be used to extract information about the density structure of the underlying (molecular) cloud, though this statement needs some qualification.

1. Flux density maps need not correspond "by eye" to column density maps: due to irradiation effects they tend to show more small-scale structure.
2. Irradiation by a point source can produce shell-like structures, mimicking physical shells, even in objects which do not have any shell-like properties.
3. As long as structure studies are restricted to areas small enough not to be contaminated by any large-scale effects, or to regions with low enough volume densities to allow volume irradiation, flux density and column density show similar structural properties. However, the application of unmodified two-point correlation functions introduces substantial errors on the mean due to the underlying anisotropy in the ISM structure.
4. MIR flux density maps tend to trace out *gradients* in the three-dimensional density distribution.

Using MIR diffuse emission to extract structure information about the underlying interstellar medium requires close attention to the environment. This study attempts to provide some guidelines to chose appropriate locations. In view of the restrictions and limitations discussed, analyzing the diffuse ISM structure with the help of the GLIMPSE data will be a formidable but possibly promising endeavor.

We are very grateful to the referee, Alyssa Goodman, for a most constructive and thorough report, and we thank E. Bergin for comments and suggestions. Computations were performed at the NCSA (AST040026) (F. H.) and on the SGI-Altix at the USM, built and maintained by M. Wetzstein and R. Gabler. Support for this work was provided by the University of Michigan (F. H.), NASA's Astrophysics Theory Program (NNG05GH35G) (B. A. W.), the *Spitzer Space Telescope* Legacy Science Program through contracts 1224988 (B. W.) and 1224653 (E. C., B. L. B., and M. R. M.) and NASA's *Spitzer Space Telescope* Fellowship Program (R. I.).

REFERENCES

Benjamin, R. A., et al. 2003, PASP, 115, 953
Bethell, T., Zweibel, E. G., Heitsch, F., & Mathis, J. S. 2004, ApJ, 610, 801
Churchwell, E., et al. 2004, ApJS, 154, 322
———. 2006, ApJ, 649, 759
Draine, B. T. 2003, ARA&A, 41, 241
Draine, B. T., & Li, A. 2006, ApJ, submitted (astro-ph/0608003)
Foster, J. B., & Goodman, A. A. 2006, ApJ, 636, L105
Górski, K. M., Hivon, E., Banday, A. J., Wandelt, B. D., Hansen, F. K., Reinecke, M., & Bartelmann, M. 2005, ApJ, 622, 759
Heitsch, F., Mac Low, M.-M., & Klessen, R. S. 2001a, ApJ, 547, 280
Heitsch, F., Slyz, A. D., Devriendt, J. E. G., & Burkert, A. 2006, MNRAS, 373, 1379
Heitsch, F., Zweibel, E. G., Mac Low, M.-M., Li, P., & Norman, M. L. 2001b, ApJ, 561, 800
Klessen, R. S., Heitsch, F., & Mac Low, M.-M. 2000, ApJ, 535, 887
Li, A., & Draine, B. T. 2001a, ApJ, 550, L213
———. 2001b, ApJ, 554, 778
Mercer, E. P., et al. 2006, ApJ, submitted
Padoan, P., Juvela, M., & Pelkonen, V.-M. 2006, ApJ, 636, L101
Reach, W. T., et al. 2006, IRAC Data Handbook (Pasadena: Caltech), http://ssc.spitzer.caltech.edu/irac/dh
Schnee, S., Bethell, T., & Goodman, A. 2006, ApJ, 640, L47
Stetson, P. B. 1987, PASP, 99, 191
Whitney, B. A., et al. 2004, ApJS, 154, 315